

REPORT DOCUMENTATION PAGE			Form Approved OMB NO. 0704-0188		
<p>The public reporting burden for this collection of information is estimated to average 1 hour per response, including the time for reviewing instructions, searching existing data sources, gathering and maintaining the data needed, and completing and reviewing the collection of information. Send comments regarding this burden estimate or any other aspect of this collection of information, including suggestions for reducing this burden, to Washington Headquarters Services, Directorate for Information Operations and Reports, 1215 Jefferson Davis Highway, Suite 1204, Arlington VA, 22202-4302. Respondents should be aware that notwithstanding any other provision of law, no person shall be subject to any penalty for failing to comply with a collection of information if it does not display a currently valid OMB control number.</p> <p>PLEASE DO NOT RETURN YOUR FORM TO THE ABOVE ADDRESS.</p>					
1. REPORT DATE (DD-MM-YYYY) 02-04-2015		2. REPORT TYPE Final Report		3. DATES COVERED (From - To) 1-Sep-2011 - 30-Nov-2014	
4. TITLE AND SUBTITLE Final Report: Topographic Optimization Through Artificial Microstructure Strategies			5a. CONTRACT NUMBER W911NF-11-1-0380		
			5b. GRANT NUMBER		
			5c. PROGRAM ELEMENT NUMBER 1D10BP		
6. AUTHORS jan schroers, Jamie Guest			5d. PROJECT NUMBER		
			5e. TASK NUMBER		
			5f. WORK UNIT NUMBER		
7. PERFORMING ORGANIZATION NAMES AND ADDRESSES Yale University Office of Grant & Contract Administration 47 College Street, Suite 203 New Haven, CT 06520 -8047			8. PERFORMING ORGANIZATION REPORT NUMBER		
9. SPONSORING/MONITORING AGENCY NAME(S) AND ADDRESS (ES) U.S. Army Research Office P.O. Box 12211 Research Triangle Park, NC 27709-2211			10. SPONSOR/MONITOR'S ACRONYM(S) ARO		
			11. SPONSOR/MONITOR'S REPORT NUMBER(S) 60700-EG-DRP.4		
12. DISTRIBUTION AVAILABILITY STATEMENT Approved for Public Release; Distribution Unlimited					
13. SUPPLEMENTARY NOTES The views, opinions and/or findings contained in this report are those of the author(s) and should not be construed as an official Department of the Army position, policy or decision, unless so designated by other documentation.					
14. ABSTRACT During this project as part of DARPA MCMA we aimed to develop and demonstrate a 3D microstructural architecture structure made from bulk metallic glass, 3DMGS, exhibiting a combination of ceramic-like high strength (>1000 MPa), metal-like high plasticity (>20%), and polymer like density (<2 g/cm ³). We developed novel processing methods such as BMG sheet fabrication and BMG joining. Topological optimization has been used to identify optimized structures for the combination of properties.					
15. SUBJECT TERMS materials, cellular structures, metallic glass					
16. SECURITY CLASSIFICATION OF:			17. LIMITATION OF ABSTRACT UU	15. NUMBER OF PAGES	19a. NAME OF RESPONSIBLE PERSON Jan Schroers
a. REPORT UU	b. ABSTRACT UU	c. THIS PAGE UU			19b. TELEPHONE NUMBER 203-432-4346

Report Title

Final Report: Topographic Optimization Through Artificial Microstructure Strategies

ABSTRACT

During this project as part of DARPA MCMA we aimed to develop and demonstrate a 3D microstructural architecture structure made from bulk metallic glass, 3DMGS, exhibiting a combination of ceramic-like high strength (>1000 MPa), metal-like high plasticity ($>20\%$), and polymer like density (<2 g/cm³). We developed novel processing methods such as BMG sheet fabrication and BMG joining. Topological optimization has been used to identify optimized structures for the combination of properties.

Enter List of papers submitted or published that acknowledge ARO support from the start of the project to the date of this printing. List the papers, including journal references, in the following categories:

(a) Papers published in peer-reviewed journals (N/A for none)

Received

Paper

09/13/2012 1.00 Baran Sarac, Jittisa Ketkaew, Dawn Olivia Popnoe, Jan Schroers. Honeycomb Structures of Bulk Metallic Glasses, Advanced Functional Materials, (08 2012): 0. doi: 10.1002/adfm.201200539

TOTAL: 1

Number of Papers published in peer-reviewed journals:

(b) Papers published in non-peer-reviewed journals (N/A for none)

Received

Paper

TOTAL:

Number of Papers published in non peer-reviewed journals:

(c) Presentations

TMS 2015
TMS 2014
MRS 2014
MRS 2013

Number of Presentations: 4.00

Non Peer-Reviewed Conference Proceeding publications (other than abstracts):

Received Paper

TOTAL:

Number of Non Peer-Reviewed Conference Proceeding publications (other than abstracts):

Peer-Reviewed Conference Proceeding publications (other than abstracts):

Received Paper

TOTAL:

Number of Peer-Reviewed Conference Proceeding publications (other than abstracts):

(d) Manuscripts

Received Paper

10/15/2013	2.00	Ze Liu, Wen Chen, Jan Schroers. joining of bulk metallic glasses in air, Acta Materiala (07 2013)
10/15/2013	3.00	Ze Liu, Wen Chen, Hannah Mae Robinson, Jan Schroers . Flaw Tolerance versus Performance: A Tradeoff in Cellular Materials, Proceedings of the National Academy of Sciences (10 2013)
TOTAL:		2

Number of Manuscripts:

Books

Received Book

TOTAL:

Received Book Chapter

TOTAL:

Patents Submitted

Liu, Z., W. Chen, J. Kaetkew, M. Kanik, R.M. Ojeda Mota, and J. Schroers, Method and equipment for thermoplastic based rolling of metallic glasses into sheets US patent application, pending, (2014).

Chen, W., Z. Liu, and J. Schroers, Method of joining metallic glasses. US patent application, (2014).

Patents Awarded

Awards

Graduate Students

<u>NAME</u>	<u>PERCENT SUPPORTED</u>	Discipline
Wen Chen	1.00	
Josephine Carstensen	1.00	
FTE Equivalent:	2.00	
Total Number:	2	

Names of Post Doctorates

<u>NAME</u>	<u>PERCENT SUPPORTED</u>	
Ze Liu	1.00	
FTE Equivalent:	1.00	
Total Number:	1	

Names of Faculty Supported

<u>NAME</u>	<u>PERCENT SUPPORTED</u>	National Academy Member
jan schroers	0.08	No
Jamie Guest	0.08	
FTE Equivalent:	0.16	
Total Number:	2	

Names of Under Graduate students supported

<u>NAME</u>	<u>PERCENT SUPPORTED</u>	Discipline
Hannah Mae Robinson	1.00	
FTE Equivalent:	1.00	
Total Number:	1	

Student Metrics

This section only applies to graduating undergraduates supported by this agreement in this reporting period

The number of undergraduates funded by this agreement who graduated during this period: 1.00

The number of undergraduates funded by this agreement who graduated during this period with a degree in science, mathematics, engineering, or technology fields:..... 1.00

The number of undergraduates funded by your agreement who graduated during this period and will continue to pursue a graduate or Ph.D. degree in science, mathematics, engineering, or technology fields:..... 0.00

Number of graduating undergraduates who achieved a 3.5 GPA to 4.0 (4.0 max scale):..... 1.00

Number of graduating undergraduates funded by a DoD funded Center of Excellence grant for Education, Research and Engineering:..... 0.00

The number of undergraduates funded by your agreement who graduated during this period and intend to work for the Department of Defense 0.00

The number of undergraduates funded by your agreement who graduated during this period and will receive scholarships or fellowships for further studies in science, mathematics, engineering or technology fields:..... 0.00

Names of Personnel receiving masters degrees

<u>NAME</u>	
Wen Chen	
Total Number:	1

Names of personnel receiving PHDs

<u>NAME</u>	
Total Number:	

Names of other research staff

<u>NAME</u>	<u>PERCENT SUPPORTED</u>
Roberto Miguel Ojeda Mota	1.00
FTE Equivalent:	1.00
Total Number:	1

Sub Contractors (DD882)

Inventions (DD882)

Scientific Progress

(Yale and Johns Hopkins)

During DARPA MCMA we aimed to develop and demonstrate a 3D microstructural architecture structure made from bulk metallic glass, 3DMGS, exhibiting a combination of ceramic-like high strength (>1000 MPa), metal-like high plasticity ($>20\%$), and polymer like density (<2 g/cm³). A benchmark material such as a structural steel exhibit plasticity of $\sim 20\%$, yield strength of 700 MPa and density of 7.9 g/cm³.

The activities can be broken down into topological optimization, fabrication, and characterization.

Fabrication of BMG 3D structures

The fabrication of BMG 3D structures requires the development of sheet fabrication methods, joining methods, and enhance existing technology on deforming BMGs.

BMG Sheet Fabrication:

Sheets of BMGs, despite their demand from industry and academia have not been available at the beginning of this project. We have been working on sheet fabrication for the last 4 years and within this program have advanced the research such that large sheets can be rolled.

The sheet fabrication is based on thermoplastic forming. The challenge is the realization of precise temperature control. Based on previous designs that we came up with in our lab we designed a large mill capable of high temperature rolling for sheet fabrication of Zr-based BMG sheets (Fig.1).

Figure 2 shows the actual realization of the equipment.

Fig. 2: High temperature rolling mill with precise temperature control, < 5 degrees. One key aspect is the pre-heating of the sheets to a temperature close but slightly lower than the rollers temperature.

In order to control temperature precisely we incorporated an active feedback mechanism. Per roller there are four thermocouples measuring temperature during the rolling process and acting as the feedback to power the heaters (Fig.3). After developing, designing, and building and first tests we researched best processing conditions for the fabrication of sheets. Specifically, we varied the pre-heat and roller temperature by 50 degrees independent from each other. We also explored the effect of area of reduction and number of passes. We took for most conditions small samples of the feedstock/sheet to characterize the state of the BMG. Here we used thermal analysis and carried out isothermal experiments which are more sensitive than constant heating experiments.

Fig. 3: Active feedback is used for temperature control and also for deformation forces (clamping forces)

Current state of the art are sheets that are ~ 15 cm by ~ 15 cm by ~ 500 microns (Fig. 4).

Figure 4: Sheets of about 15 cm in diameter and 0.5 mm in thickness can be readily formed with described rolling mill and optimized processing conditions from Zr-BMG.

Joining of BMG sheets:

Joining methods like welding or diffusion bonding, typically used for crystalline metals are not applicable for BMGs. We developed a completely new concept of joining BMGs which is based on oxide cracking through surface straining.

The joining strategies are summarized in Fig.5. We considered three different strategies, shearing, squeezing, and oxide pulling.

•

For all BMG joining processes we have considered two BMGs are sheared at a temperature of the supercooled liquid region against each other. Deformation breaks the oxide layer and creates a fresh surface. The idea is that the fresh surface area forms a chemical bond with the same bond strength than the BMGs strength. The overall strength of the joint is given by the area of fresh surface normalized by the overall area of the joint. So in theory one can achieve bond strength from ~1800 MPa (all fresh surface) to 0 MPa if the oxide layer is not broken.

Most advanced is our joining by squeezing technique (Fig.6). Here we join two BMG parts by heating into the supercooled liquid region, and we can do this in air, and simultaneously force them against each other. The BMG deforms and so does the interface. The increase surface area is the joined surface and the ratio of new to old surface area defines by the rule of mixing the strength of the interface. We characterize the bond shear-strength according to the method describe in Figure 7.

We characterized the interfaces through shear stress determination (Fig. 8). In addition we employed SEM. The SEM images confirmed our hypothesis and suggested other techniques than our original shearing technique.

Once the oxide layer is removed a chemical bond forms of the same strength than the BMG strength. This is furthermore confirmed in Figure 9 where the interface fractures in a complete ductile manner, showing a typical vein pattern. Only the areas where the oxide layer has not been removed do not bond.

3DMGMA fabrication:

The development of a BMG sheet fabrication method and the joining of the sheets has been a requirement for the fabrication of 3DMGMA structures.

The sheets are deformed through a thermoplastic-based deformation method into corrugated structures (Fig. 10b). In a subsequent processing step such structures are joined together through the above-described joining (Fig.10c). This process is fast, scaleable, and can be carried out in air. After removing of the space holders, the 3DMGMA structure is finalized. Our current setup is not build to fabricate significantly larger samples than shown, but in principle our method allows to fabricate much larger scale structures (Fig.11).

Fig. 10 BMG 3D structures fabrication processes: (a) Starting BMG sheets (①). (b) Patterned BMG sheets by using thermoplastic molding (②). (c) Joining patterned BMG sheets by heating. (d) 3D structures after demoulding (③).

Fig. 11 Examples of the numerous 3DMGMA that we fabricated.

Modeling and Topological Optimization of 3D microstructures

The theoretical aspect of this project focused on quality models capable of capturing the response of the 3D bonded microstructures, including collapse mechanisms and system sensitivity to bonding locations and properties.

Figure 12 displays an example model of the NavTruss architecture, with layers oriented in a staggered pattern and bonded ('welds') at the interface. Figure 13 shows the resulting stress-strain response under compression for bond strength varying

from 100% of the BMG sheet material to 25%. The plot shows that the overall material system response is relatively consistent for bond strengths of 50%, 75%, and 100%, although for the case of 50% bond strength yielding is initiated in the welds, leading to slightly lower peak strength. The case of 25% bond strength, however, exhibited significantly lower peak strength and effective stiffness, as the welds yielded entirely before reaching loads at which the plate walls would buckle. This suggests that bond strengths achieving at least 50% of the base BMG sheet material are sufficient to prevent premature failure of the welds.

Figure 12. 3D representation of alternating NavTruss architecture highlighting the bonding material phase whose properties can be varied to explore system sensitivity.

Figure 13. Stress-strain response and corresponding failure mechanisms for the alternating NavTruss architecture assuming: (left) perfect bonding and (right) bond strength is 50% of the base BMG sheet material. Note that the mechanisms change slightly but the overall effect on strength is minor for bond strengths greater than 25% of the base material.

Figure 14 displays the effect on the stress-strain response of varying the angle of corrugation, within the range at which the fabrication team was initially investigating. Although the range is relatively small at ten degrees, it is interesting to note that the initial failure mechanism and location moves from buckling of the plates in the 90 degree corrugation case to yielding in the welds in the 80 degree case. As the plot shows, this translates into the 90 degree case losing stiffness at a smaller strain due to buckling, but exhibiting a higher strength post-buckling as the material remains elastic at larger strains than the 80 degree case.

Figure 14. Stress-strain response for the alternating NavTruss architecture with varying angles of corrugation.

Figure 15 illustrates the stress-strain response under varying sheet thicknesses. Increasing sheet thickness delays the onset of buckling and thus correlates to material peak strength and stiffness, but also failure under smaller strains. We are currently attempting to develop analytical expressions that account for the layer bonding to enable efficient design of these structures.

Figure 15: Numerically obtained stress-strain curves for 3D hexagonal folded sheets with relative densities of 11.4%, 10%, 8% and 6% (2D cross-sections shown).

In addition to strength modeling of the 3D corrugated systems, we have also been enhancing our models to capture post-peak performance, including layer collapse, contact, and densification. This provides a more realistic prediction of energy absorption that we intend to include in the optimization routines. Due to the high computational expense, we first develop these models using our 2D topologies optimized for energy absorption (Figure 16).

Figure 16: Cellular BMG sample of the tested sample of the 12.5% optimized unit cell design with scale bar 1mm, magnified view with scale bar 200 μm .

The experimental and numerical results are compared for the topology-optimized 12.5% relative density sample in Figure 17. The strengths observed in the tests are higher for the base materials, which may be due to the assumed base material properties or slight modifications in topology to prepare the CAD file. However, the overall shapes of the curves are remarkably similar, including the strains at which the first two major peaks occur, and the very small peak and valley in between the two major peaks. These similarities have allowed us to look in detail at how the deformation evolves following initial yielding. The deformation sequence is shown in Figure 18 - the steep decent after the initial peak is found to be caused by fracture of a member followed by densification of a layer of unit cells. This process is repeated and causes the stress-strain response to oscillate. Remarkably, the stiffness leading to and strength at the second peak are nearly identical to the initial, undamaged material (zoom-in of Figure 9).

These new modeling capabilities have improved our understanding of these complex, bonded material systems and will enable future optimization for properties beyond the currently considered sets of elastic stiffness, peak strength, and energy absorption to first peak.

Figure 17: Experimental and numerical stress-strain responses of 12.5% optimized samples in BMG, demonstrating the models are capable of capturing the post-peak response.

Figure 18: Numerically predicted deformation of the BMG12.5% relative density sample. Note the stiffness and strength at the second peak are nearly the same as the undamaged state.

Characterization of 3DMGMA

We characterized the 3DMGMA fabricated according to the process laid out in Fig.1 through quasi-static compression. Figure 19 shows one example of where the relative density of the 3D BMG is $\rho/\rho_s = 0.073$. Some selected frames from the in-situ recording movie are plotted in the inset. The structure first undergoes elastic deformation (Fig. 19① and ②), then gradually yields around joint points of walls (Fig. 19③-⑦) and finally enters the densification region (Fig. 19⑧). After unloading, the structure partially recovers (Fig. 19 ⑨). This significant recovery shows that fracture occurs in the ligament but not in the joint sites, which confirms the high and predictable joint strength and ductility of BMG walls.

Fig. 19 Characterization of 3DMGMA with density of 0.39 g/cm³.

Ideal mechanic responses of BMG 3D structures from finite element analysis (FEA).

We also simulated the ideal behavior of considered structures and how this behavior deviates from the experimentally observed (Fig. (20)). Origins of the underperforming compare to simulation predictions are the non-uniformity of the wall thicknesses in experiments and to some extent the difficulty of matching the boundary conditions of experiments with simulations.

Fig. 20 Comparison of experimental results with simulations.

Fig. 21 (a) Unit honeycomb cell under uni-axial compression. (b) Bending dominated elastic deformation.

Ultra-elasticity of BMG 3D honeycomb structures

We observed a very large elastic response of the 3D BMG structures. Theoretically one can describe elastic behavior of 3D structure as follows:

For a honeycomb 3D structure under uni-axial compression, the unit cell is shown in Fig.21 (a). Elastic deformation is dominated by the bending of the side walls. The deflection of the side wall can be approximated by (Fig. 21 (b))

(1)

And the maximum curvature is

(2)

While plastic yielding starts when

(3)

where h is the thickness of beam and ϵ_{cr} is the elastic limit of solid material. Combining eq. (2) and eq. (3) gives

(4)

For bending dominated deformation, the axial deformation is negligible, we have

(5)

where $\lambda = L'/L$, L is the initial length of beam. And the maximum apparent elastic strain is thus

(6)

Eqs. (5) and (6) give the maximum elasticity of 3D structures for different materials, aspect ratio (or porosity) and tilt angle of the walls (θ). For regular honeycomb structures, $\theta = 30^\circ$, Porosity = $P = 1 - \rho/\rho_s$.

For the structure shown in Fig. 10, the measured maximum apparent elastic strain is ~14%, which is close to the theoretical prediction of 17% (From eqs. (5) and (6)) (Fig.22). As a consequence 3D structures made from BMGs yield dramatically higher elasticity than 3D structures made from other structural materials.

Fig. 22 Maximum elasticity of 3D honeycomb structures. Solid lines – theoretical predictions.

Technology Transfer

Final Report for: Topological Optimization of Artificial Microstructure Strategies

(Yale and Johns Hopkins)

During DARPA MCMA we aimed to develop and demonstrate a 3D microstructural architecture structure made from bulk metallic glass, 3DMGS, exhibiting a combination of ceramic-like high strength (>1000 MPa), metal-like high plasticity ($>20\%$), and polymer like density (<2 g/cm³). A benchmark material such as a structural steel exhibit plasticity of $\sim 20\%$, yield strength of 700 MPa and density of 7.9 g/cm³.

The activities can be broken down into topological optimization, fabrication, and characterization.

Fabrication of BMG 3D structures

The fabrication of BMG 3D structures requires the development of sheet fabrication methods, joining methods, and enhance existing technology on deforming BMGs.

BMG Sheet Fabrication:

Sheets of BMGs, despite their demand from industry and academia have not been available at the beginning of this project. We have been working on sheet fabrication for the last 4 years and within this program have advanced the research such that large sheets can be rolled.

The sheet fabrication is based on thermoplastic forming. The challenge is the realization of precise temperature control. Based on previous designs that we came up with in our lab we designed a large mill capable of high temperature rolling for sheet fabrication of Zr-based BMG sheets (Fig.1).

Figure 2 shows the actual realization of the equipment.

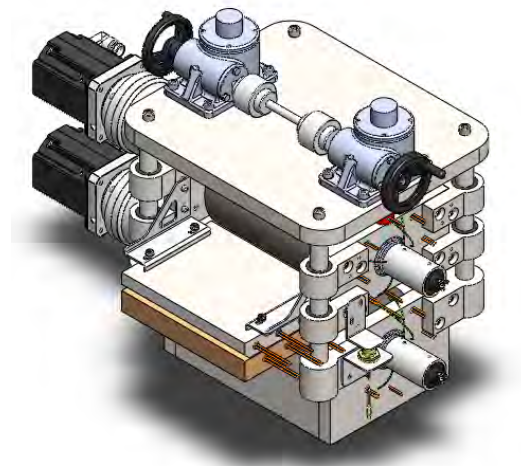


Fig. 1: Schematics of our new rolling mill to fabricate 3D BMG structures.

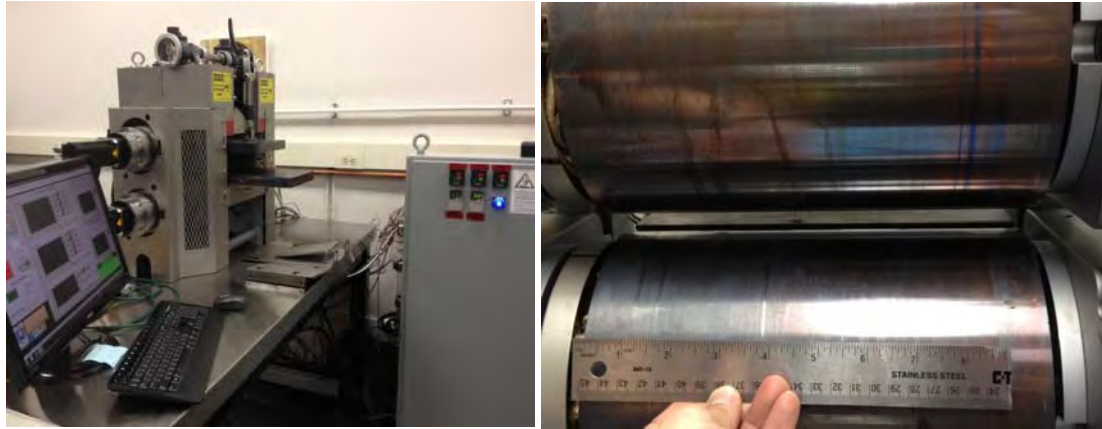


Fig. 2: High temperature rolling mill with precise temperature control, < 5 degrees. One key aspect is the pre-heating of the sheets to a temperature close but slightly lower than the rollers temperature.

In order to control temperature precisely we incorporated an active feedback mechanism. Per roller there are four thermocouples measuring temperature during the rolling process and acting as the feedback to power the heaters (Fig.3). After developing, designing, and building and first tests we researched best processing conditions for the fabrication of sheets. Specifically, we varied the pre-heat and roller temperature by 50 degrees independent from each other. We also explored the effect of area of reduction and number of passes. We took for most conditions small samples of the feedstock/sheet to characterize the state of the BMG. Here we used thermal analysis and carried out isothermal experiments which are more sensitive than constant heating experiments.

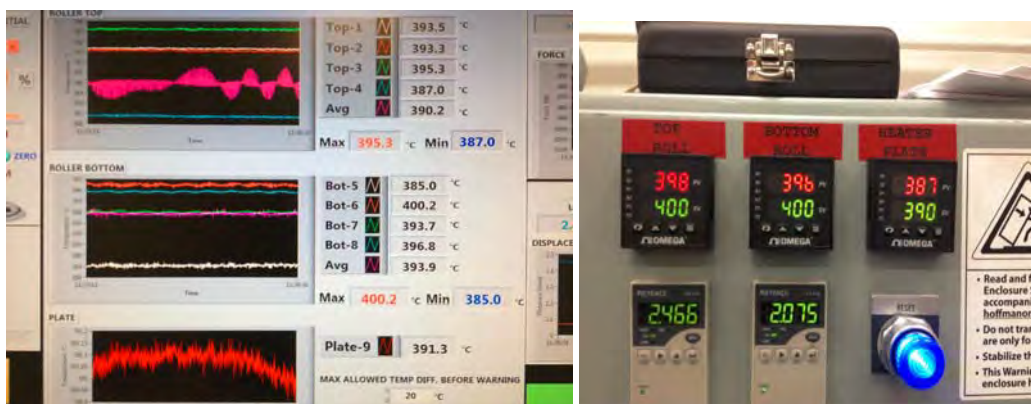


Fig. 3: Active feedback is used for temperature control and also for deformation forces (clamping forces)

Current state of the art are sheets that are ~15 cm by ~15 cm by ~ 500 microns (Fig. 4).



Figure 4: Sheets of about 15 cm in diameter and 0.5 mm in thickness can be readily formed with described rolling mill and optimized processing conditions from Zr-BMG.

Joining of BMG sheets:

Joining methods like welding or diffusion bonding, typically used for crystalline metals are not applicable for BMGs. We developed a completely new concept of joining BMGs which is based on oxide cracking through surface straining.

The joining strategies are summarized in Fig.5. We considered three different strategies, shearing, squeezing, and oxide pulling.

•

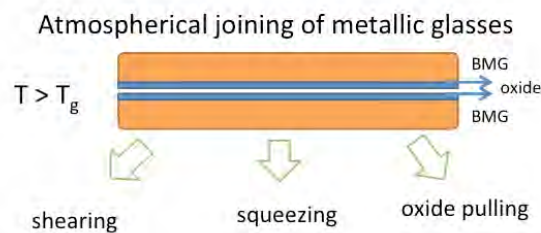


Fig.5: Schematics of joining strategies of metallic glasses.

For all BMG joining processes we have considered two BMGs are sheared at a temperature of the supercooled liquid region against each other. Deformation breaks the oxide layer and creates a fresh surface. The idea is that the fresh surface area forms a chemical bond with the same bond strength than the BMGs strength. The overall strength of the joint is given by the area of fresh surface normalized by the overall area of the joint. So in theory one can achieve bond strength from ~1800 MPa (all fresh surface) to 0 MPa if the oxide layer is not broken.

Most advanced is our joining by squeezing technique (Fig.6). Here we join two BMG parts by heating into the supercooled liquid region, and we can do this in air, and simultaneously force them against each other. The BMG deforms and so does the interface. The increase surface area is the joined surface and the ratio of new to old surface area defines by the rule of mixing the strength of the interface. We characterize the bond shear-strength according to the method describe in Figure 7.

Atmospherical joining of metallic glasses ---- squeezing

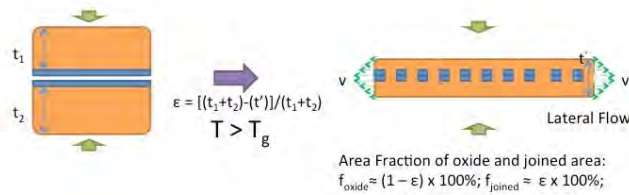


Fig.6: Schematics of joining by squeezing of metallic glasses.

Joint Reliability Characterization for Squeezing Joining

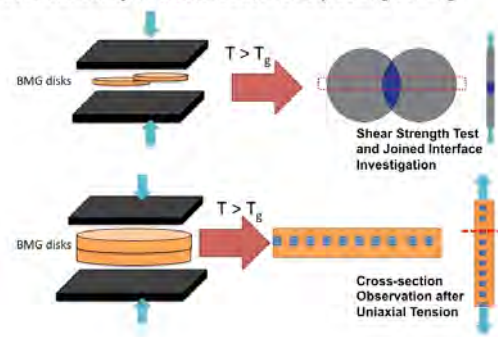


Fig.7: Schematics of the characterization method of the interface strength.

We characterized the interfaces through shear stress determination (Fig. 8). In addition we employed SEM. The SEM images confirmed our hypothesis and suggested other techniques than our original shearing technique.

Once the oxide layer is removed a chemical bond forms of the same strength than the BMG strength. This is furthermore confirmed in Figure 9 where the interface fractures in a complete ductile manner, showing a typical vein pattern. Only the areas where the oxide layer has not been removed do not bond.

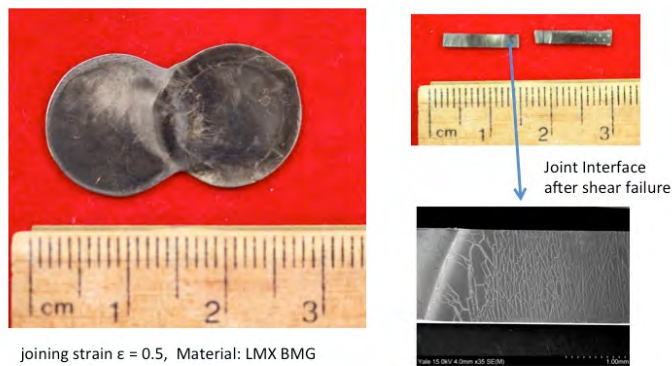


Fig. 8: Joint interface fabricated by the squeezing technique.

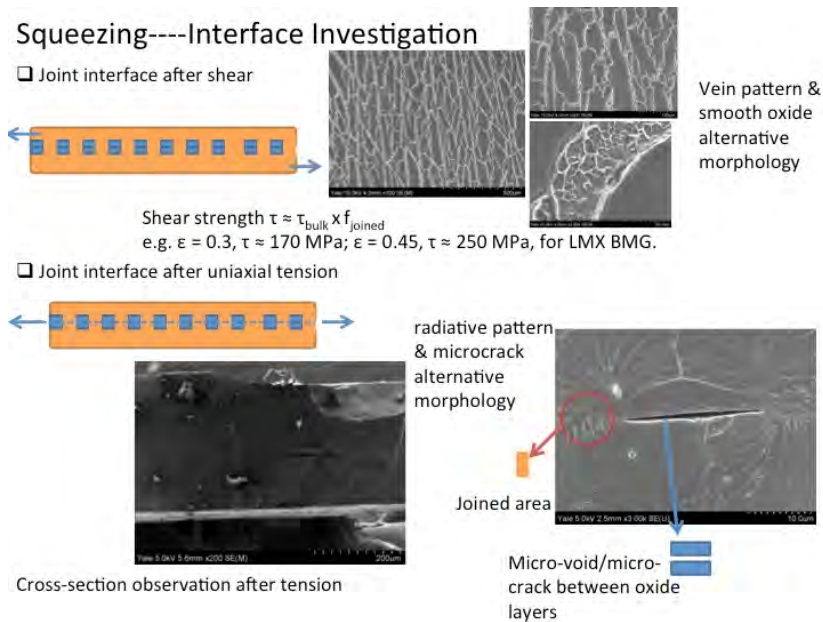


Fig. 9: Interface structure after failure indicate a strong chemical bond of magnitude similar of the strength of the BMG and no bond for the interface regions that are still covered by an oxide layer.

3DMGMA fabrication:

The development of a BMG sheet fabrication method and the joining of the sheets has been a requirement for the fabrication of 3DMGMA structures.

The sheets are deformed through a thermoplastic-based deformation method into corrugated structures (Fig. 10b). In a subsequent processing step such structures are joined together through the above-described joining (Fig.10c). This process is fast, scaleable, and can be carried out in air. After removing of the space holders, the 3DMGMA structure is finalized. Our current setup is not build to fabricate significantly larger samples than shown, but in principle our method allows to fabricate much larger scale structures (Fig.11).

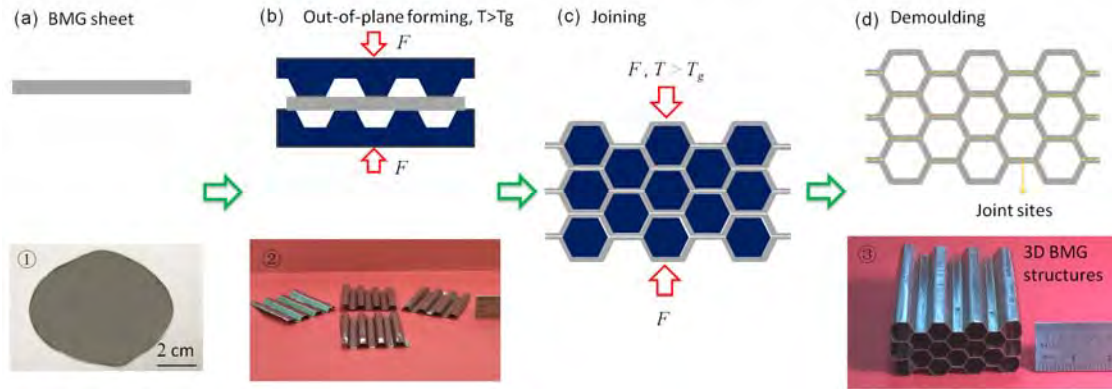


Fig. 10 BMG 3D structures fabrication processes: (a) Starting BMG sheets (①). (b) Patterned BMG sheets by using thermoplastic molding (②). (c) Joining patterned BMG sheets by heating. (d) 3D structures after demoulding (③).

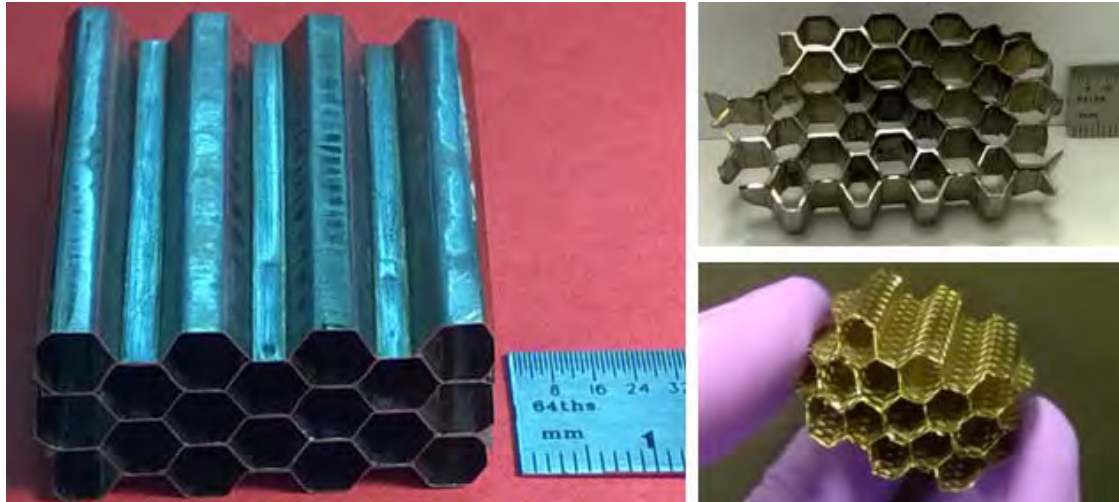


Fig. 11 Examples of the numerous 3DMGMA that we fabricated.

Modeling and Topological Optimization of 3D microstructures

The theoretical aspect of this project focused on quality models capable of capturing the response of the 3D bonded microstructures, including collapse mechanisms and system sensitivity to bonding locations and properties.

Figure 12 displays an example model of the NavTruss architecture, with layers oriented in a staggered pattern and bonded ('welds') at the interface. Figure 13 shows the resulting stress-strain response under compression for bond strength varying from 100% of the BMG sheet material to 25%. The plot shows that the overall material system response is relatively consistent for bond strengths of 50%, 75%, and 100%, although for the case of 50% bond strength yielding is initiated in the welds, leading to slightly lower peak strength. The case of 25% bond strength, however, exhibited significantly lower peak strength and effective stiffness, as the welds yielded entirely before reaching loads at which the plate walls would buckle. This suggests that bond strengths achieving at least 50% of the base BMG sheet material are sufficient to prevent premature failure of the welds.

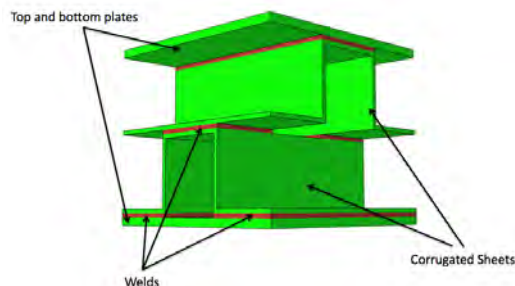


Figure 12. 3D representation of alternating NavTruss architecture highlighting the bonding material phase whose properties can be varied to explore system sensitivity.

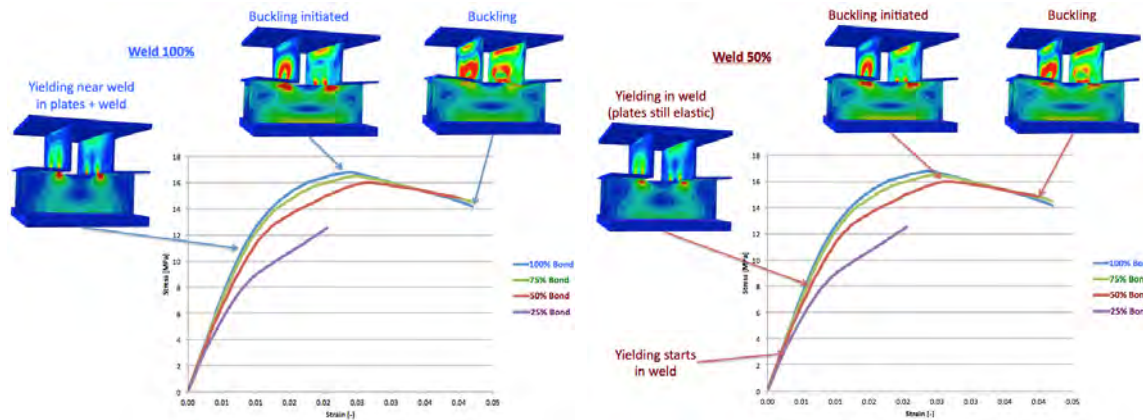


Figure 13. Stress-strain response and corresponding failure mechanisms for the alternating NavTruss architecture assuming: (left) perfect bonding and (right) bond strength is 50% of the base BMG sheet material. Note that the mechanisms change slightly but the overall effect on strength is minor for bond strengths greater than 25% of the base material.

Figure 14 displays the effect on the stress-strain response of varying the angle of corrugation, within the range at which the fabrication team was initially investigating. Although the range is relatively small at ten degrees, it is interesting to note that the initial failure mechanism and location moves from buckling of the plates in the 90 degree corrugation case to yielding in the welds in the 80 degree case. As the plot shows, this translates into the 90 degree case losing stiffness at a smaller strain due to buckling, but exhibiting a higher strength post-buckling as the material remains elastic at larger strains than the 80 degree case.

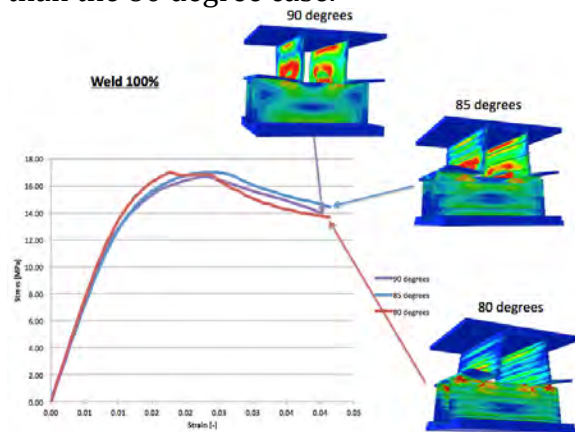


Figure 14. Stress-strain response for the alternating NavTruss architecture with varying angles of corrugation.

Figure 15 illustrates the stress-strain response under varying sheet thicknesses. Increasing sheet thickness delays the onset of buckling and thus correlates to material peak strength and stiffness, but also failure under smaller strains. We are currently attempting to develop analytical expressions that account for the layer bonding to enable efficient design of these structures.

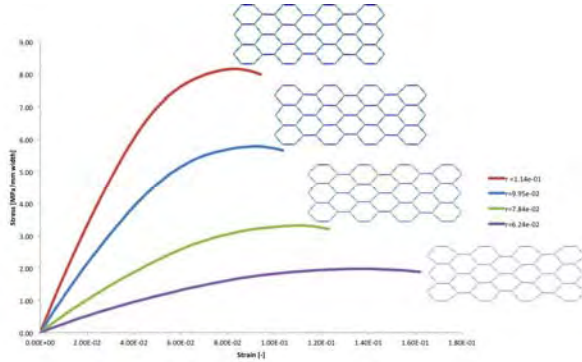


Figure 15: Numerically obtained stress-strain curves for 3D hexagonal folded sheets with relative densities of 11.4%, 10%, 8% and 6% (2D cross-sections shown).

In addition to strength modeling of the 3D corrugated systems, we have also been enhancing our models to capture post-peak performance, including layer collapse, contact, and densification. This provides a more realistic prediction of energy absorption that we intend to include in the optimization routines. Due to the high computational expense, we first develop these models using our 2D topologies optimized for energy absorption (Figure 16).

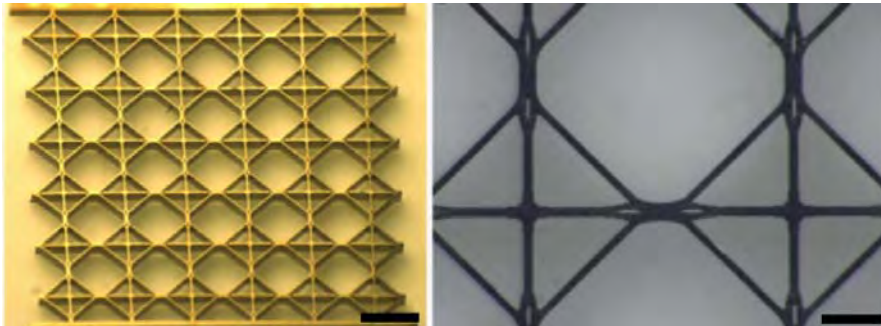
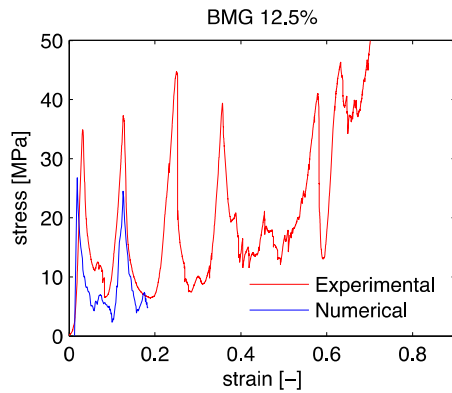


Figure 16: Cellular BMG sample of the tested sample of the 12.5% optimized unit cell design with scale bar 1mm, magnified view with scale bar 200 μm.

The experimental and numerical results are compared for the topology-optimized 12.5% relative density sample in Figure 17. The strengths observed in the tests are higher for the base materials, which may be due to the assumed base material properties or slight modifications in topology to prepare the CAD file. However, the overall shapes of the curves are remarkably similar, including the strains at which the first two major peaks occur, and the very small peak and valley in between the two major peaks. These similarities have allowed us to look in detail at how the deformation evolves following initial yielding. The deformation sequence is shown in Figure 18 - the steep decent after the initial peak is found to be caused by fracture of a member followed by densification of a layer of unit cells. This process is repeated and causes the stress-strain response to

oscillate. Remarkably, the stiffness leading to and strength at the second peak are nearly identical to the initial, undamaged material (zoom-in of Figure 9).

These new modeling capabilities have improved our understanding of these complex, bonded material systems and will enable future optimization for properties beyond the currently considered sets of elastic stiffness, peak strength, and energy absorption to first peak.



6 optimized
e post-peak

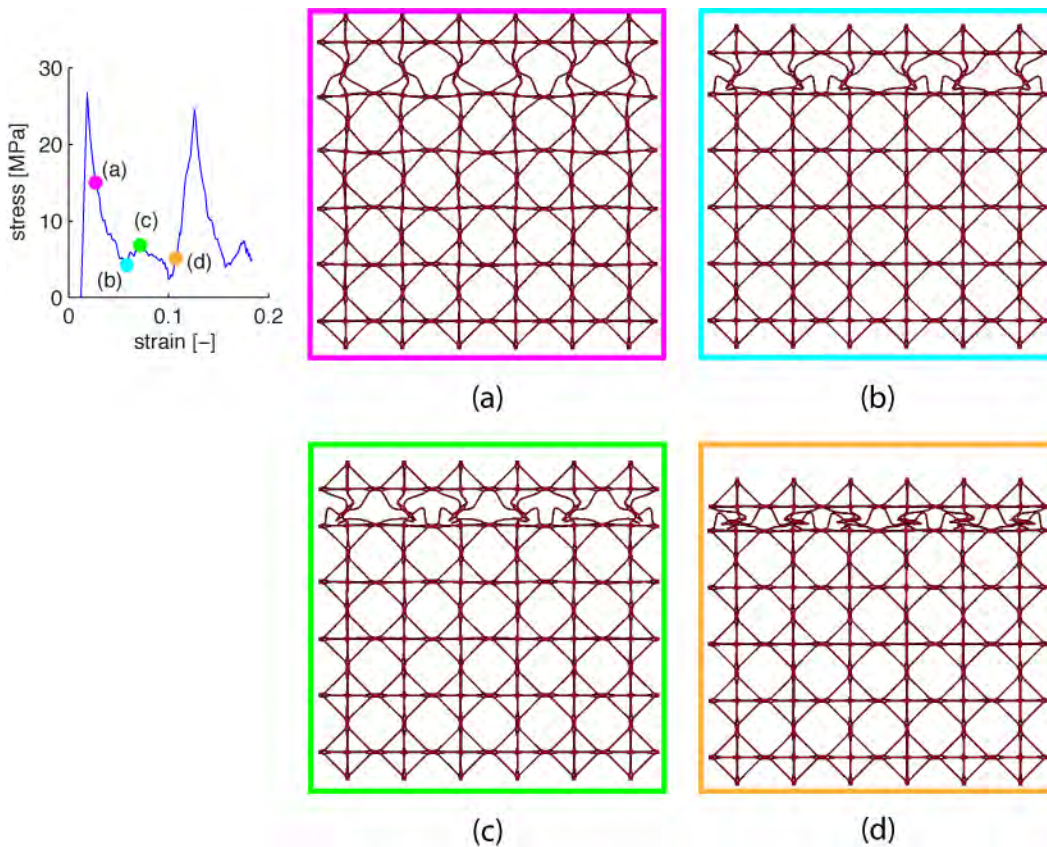


Figure 18: Numerically predicted deformation of the BMG12.5% relative density sample. Note the stiffness and strength at the second peak are nearly the same as the undamaged state.

Characterization of 3DMGMA

We characterized the 3DMGMA fabricated according to the process laid out in Fig.1 through quasi-static compression. Figure 19 shows one example of where the relative density of the 3D BMG is $\rho/\rho_s = 0.073$. Some selected frames from the in-situ recording movie are plotted in the inset. The structure first undergoes elastic deformation (Fig. 19① and ②), then gradually yields around joint points of walls (Fig. 19③–⑦) and finally enters the densification region (Fig. 19⑧). After unloading, the structure partially recovers (Fig. 19⑨). This significant recovery shows that fracture occurs in the ligament but not in the joint sites, which confirms the high and predictable joint strength and ductility of BMG walls.

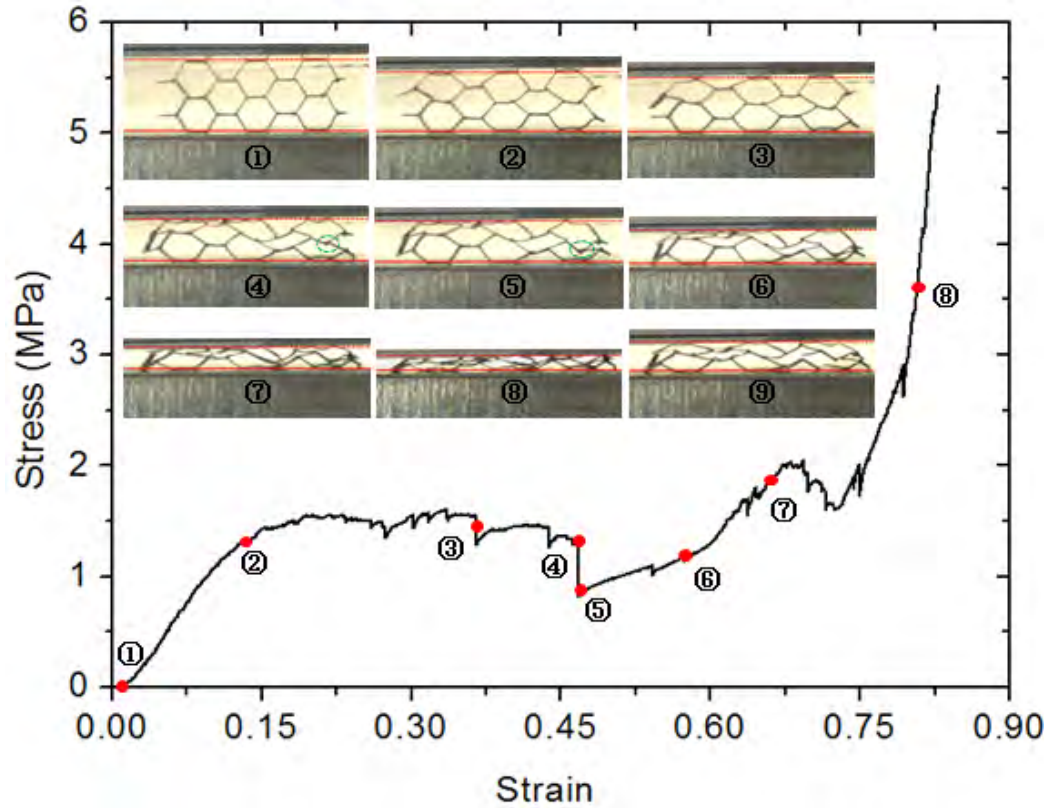


Fig. 19 Characterization of 3DMGMA with density of 0.39 g/cm³.

Ideal mechanic responses of BMG 3D structures from finite element analysis (FEA).

We also simulated the ideal behavior of considered structures and how this behavior deviates from the experimentally observed (Fig. (20). Origins of the underperforming compare to simulation predictions are the non-uniformity of the wall thicknesses in

experiments and to some extent the difficulty of matching the boundary conditions of experiments with simulations.

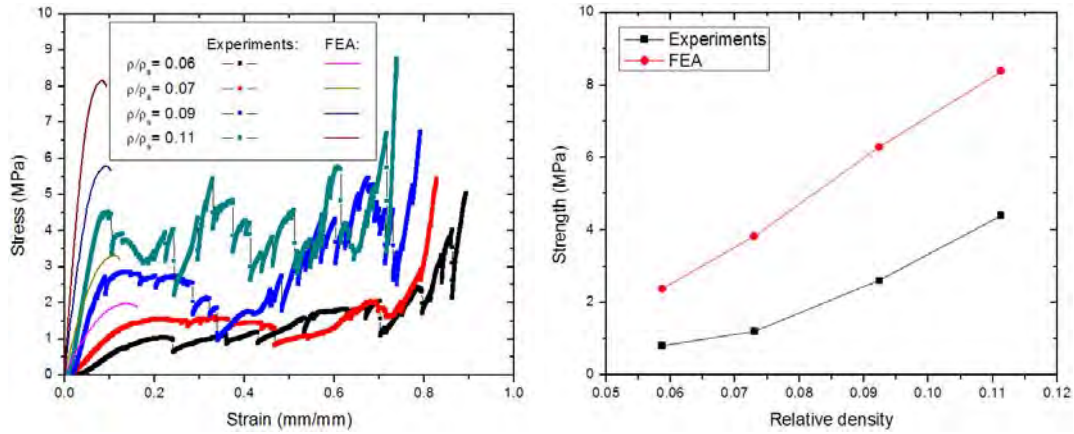


Fig. 20 Comparison of experimental results with simulations.

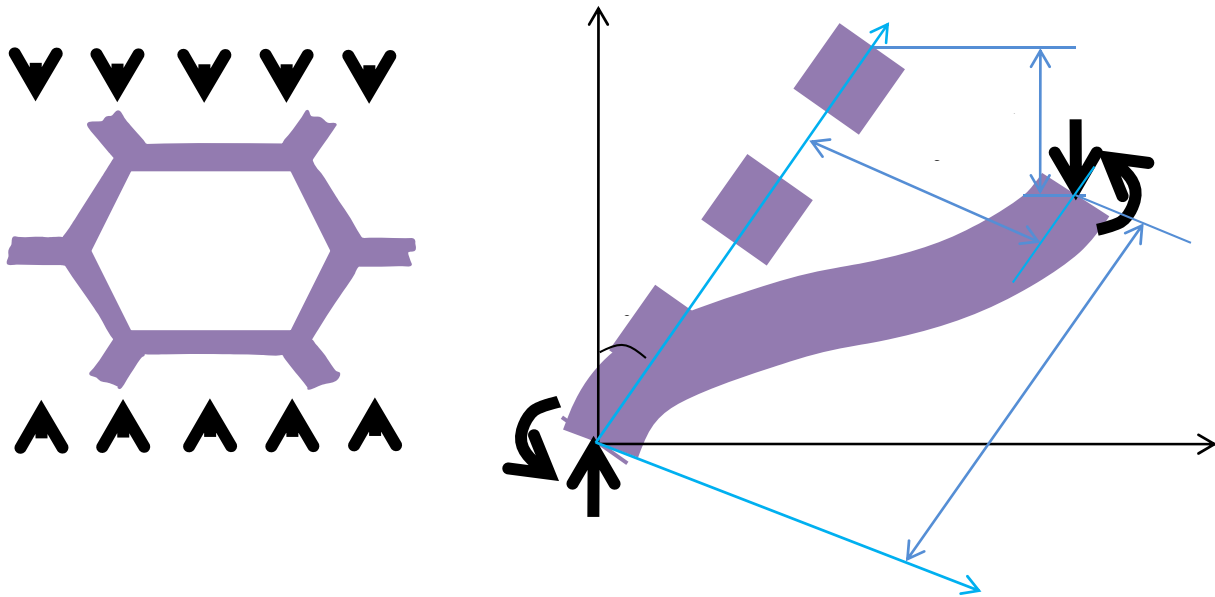


Fig. 21 (a) Unit honeycomb cell under uni-axial compression. (b) Bending dominated elastic deformation.

Ultra-elasticity of BMG 3D honeycomb structures

We observed a very large elastic response of the 3D BMG structures. Theoretically one can describe elastic behavior of 3D structure as follows:

For a honeycomb 3D structure under uni-axial compression, the unit cell is shown in Fig.21 (a). Elastic deformation is dominated by the bending of the side walls. The deflection of the side wall can be approximated by (Fig. 21 (b))

$$y' = \frac{\delta}{2} \left(1 - \cos \left(\frac{\pi}{L'} x' \right) \right) \quad (1)$$

And the maximum curvature is

$$k_{\max} = \frac{\pi^2 \delta}{2L'^2} \quad (2)$$

While plastic yielding starts when

$$k_{\max} = \frac{2\varepsilon_{\text{cr}}}{h} \quad (3)$$

where h is the thickness of beam and ε_{cr} is the elastic limit of solid material. Combining eq. (2) and eq. (3) gives

$$\delta = \frac{4\varepsilon_{\text{cr}} L'^2}{\pi^2 h} \quad (4)$$

For bending dominated deformation, the axial deformation is negligible, we have

$$\frac{1}{\lambda} = \int_0^1 \sqrt{1 + \frac{4\varepsilon_{\text{cr}}^2}{\pi^2} \left(\frac{L}{h} \right)^2 \lambda^2 \sin^2(\pi\zeta)} d\zeta \quad (5)$$

where $\lambda = L'/L$, L is the initial length of beam. And the maximum apparent elastic strain is thus

$$\varepsilon_{\text{ap},\max} = 1 - \lambda + \frac{4\varepsilon_{\text{cr}}}{\pi^2} \frac{L}{h} \lambda^2 \tan \theta \quad (6)$$

Eqs. (5) and (6) give the maximum elasticity of 3D structures for different materials, aspect ratio (or porosity) and tilt angle of the walls (θ). For regular honeycomb structures, $\theta = 30^\circ$, Porosity = $P = 1 - \rho/\rho_s$.

For the structure shown in Fig. 10, the measured maximum apparent elastic strain is $\sim 14\%$, which is close to the theoretical prediction of 17% (From eqs. (5) and (6)) (Fig.22). As a consequence 3D structures made from BMGs yield dramatically higher elasticity than 3D structures made from other structural materials.

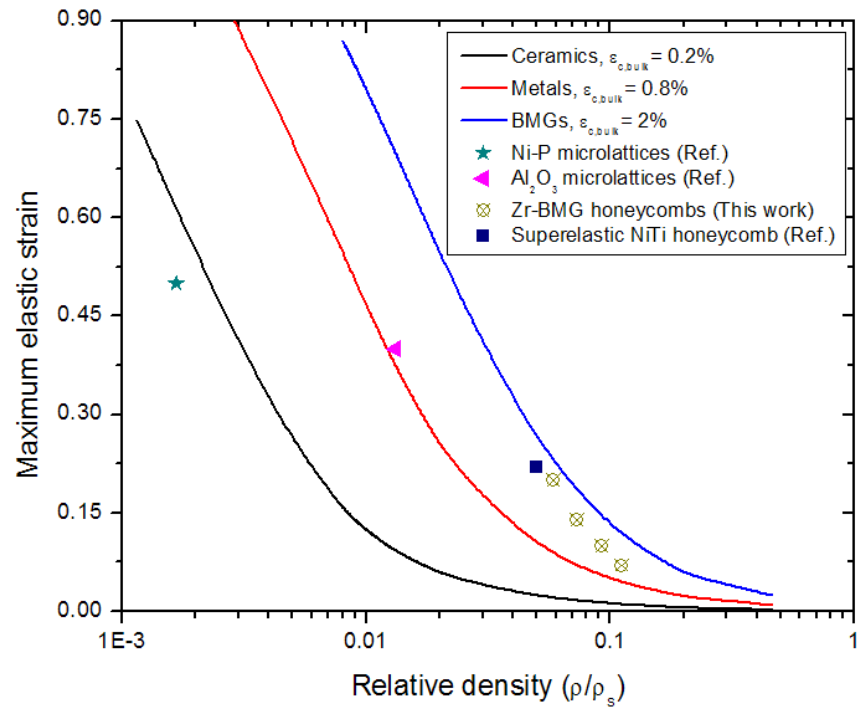


Fig. 22 Maximum elasticity of 3D honeycomb structures. Solid lines – theoretical predictions.